nanomaterials

MDPI

Article

Real-Time Analysis of Laser-Induced Plasmon Tuning in Nanoporous Glass Composite

Maksim M. Sergeev [1], Roman A. Zakoldaev [1,*], Tatiana E. Itina [1,2], Pavel V. Varlamov [1] and Galina K. Kostyuk [1]

[1] Faculty of Laser Photonics and Optoelectronics, ITMO University, 197101 Saint Petersburg, Russia; mmsergeev@itmo.ru (M.M.S.); tatiana.itina@univ-st-etienne.fr (T.E.I.); p.v.varlamov@itmo.ru (P.V.V.); gkkostiuk@itmo.ru (G.K.K.)

[2] Laboratoire Hubert Curien, UMR CNRS 5516/UJM/Univ. Lyon, Bat. F, 18 rue du Pr. Benoit Lauras, 42000 Saint-Etienne, France

* Correspondence: zakoldaev@itmo.ru; Tel.: +7-911-144-52-56

Received: 5 May 2020; Accepted: 4 June 2020; Published: 8 June 2020

Abstract: Laser-induced structuring in nanoporous glass composites is promising for numerous emerging applications in photonics and plasmonics. Local laser irradiation activates an interplay of photo-thermo-chemical mechanisms that are extremely difficult to control. The choice of optimum laser parameters to fabricate structures with desired properties remains extremely challenging. Another challenging issue is the investigation of the properties of laser-induced buried structures. In this paper, we propose a way to control the plasmonic structures formation inside a nanoporous glass composite with doped silver/copper ions that are induced by laser irradiation. Experimental and numerical investigations both demonstrate the capacities of the procedure proving its validity and application potential. In particular, we register transmitted laser power to analyse and control the modification process. Spectral micro-analysis of the irradiated region shows a multilayer plasmonic structure inside the glass composite. Subsequently, the effective medium theory connects the measured spectral data to the numerically estimated size, concentration, and chemical composition of the secondary phase across the initial GC sample and the fabricated structure.

Keywords: nanocomposites; porous glass; laser writing; plasmon resonance; nanoparticles; effective medium theory

1. Introduction

New functional glass composites with embedded nanoparticles are applied in photonics [1,2] in order to fabricate nonlinear light guiding components [3], luminescent [4], and plasmonic [5] structures, bimetallic nanoparticles [6], or colour palettes [7]. Particularly, nanoporous glass with multiple buried hollow channels and pores with well-controlled size represents a promising base for glass composite development [8]. Such a nanoporous framework captures a wide class of dopants: silver halides [9], rare-earth metals [10], or nanoparticles [11]. Laser treatment changes the internal structure of a nanoporous glass composite and tunes its plasmonic properties. However, laser irradiation initiates high-rate photo-thermal-chemical mechanisms [12], which complicate the search for optimal irradiation modes.

Generally, laser irradiation forms a buried modified region in a nanoporous glass composite, more specifically a multilayer spherical plasmonic structure with the concentration of nanoparticles distributed across the cross-section [13]. Moreover, processes, such as growth [14], fragmentation [15], and reduction or oxidation of nanoparticles occur in the irradiated zone, thus defining the structure optical properties that are commonly measured after laser processing by contact examination. However,

this approach to measurements remains semi-empirical and cannot explain all of the physical and chemical transformations involved.

Obviously, the real-time investigation of micro-sized buried structures is preferable during laser irradiation. The determination of the optical characteristics, such as refractive index, extinction, and absorption coefficient of the structure, remains challenging. For this, we develop a procedure allowing for one to predict the optical properties of fabricated structures and determine the required laser exposure time and power.

Several optical models, such as Maxwell-Garnett [16] and Burgemann-Bergman [17], were used to simulate optical properties of the glass composite. Additionally, Mie theory and Clausius–Mossotti equation were also used [18]. For simplicity of simulation, the processes of nanoparticle formation, growth, and decay/oxidation were, however, often neglected. Nevertheless, laser irradiation inevitably causes these processes creating additional conditions in the simulation.

Herein, we propose a novel real-time control procedure combining both experimental investigation and simulation to fabricate micro-sized structures inside nanoporous glass doped with silver and copper ions by laser irradiation. In particular, we propose a model that accounts for the time dependent changes in the optical properties during laser irradiation. This procedure requires the registration of the transmitted laser power by power detectors in combination with a careful numerical simulation, which makes the procedure low-cost and easily implementable. For this, we have chosen to simulate plasmonic properties using the effective medium theory (EMT) [19], as this approach is the most relevant under the considered experimental conditions. Experimentally, spectral non-contact measurements are used here to obtain the size, concentration, and chemical composition of the secondary phase across the fabricated structure. Furthermore, physical mechanisms of laser radiation interaction with a nanoporous glass composite are also discussed.

2. Materials, Laser Procedure and Modelling

2.1. Materials

In the experiment, a plane-parallel glass composite (GC) sample with 1.5 mm thickness is subjected to the near-infrared continuous wave (CW) laser irradiation procedure. GC based on a porous glass (PG) is impregnated with silver/copper halides in the ratio 1:10. Note that the average pores radius, which is around 4 nm and 26% of the total porosity, limits the halides size up to 12 nm [20]. GC chemical composition is the following: 0.25 Na_2O – 3.42 B_2O_3 – 96.09 SiO_2 – 0.24 Ag_2O. The sample preparation is a complex and multi-stage procedure, which includes PG fabrication that is based on two-phase alkali borosilicate glass thermal treatment and the following chemical etching to delete a borate phase [21,22]. The final impregnation procedure with silver/copper halides is described elsewhere [23]. Here, we consider a silicate matrix with embedded ions of Na and B in terms of residual trace elements and nanopores filled with Ag/Cu ions.

An additional three samples, such as PG without any dopants, fully sintered GC (SGC) [24], and fused silica (FS), are applied as the reference samples for the simulation stage. Sample transmittance and reflectance are measured in the range from 0.3 to 1.1 μm by a spectrophotometer (MSFU-K Yu-30.54.072, LOMO, St. Petersburg, Russia), where the minimum registration region is equal to 2 μm (Figure 1). The transmittance T_{meas} and reflectance R_{meas} of all the samples are measured at normal incidence of light. Spectral curves show that initial PG is similar to FS, except for the UV absorption. Introducing halides in the PG results in a significant absorption in the range from 0.45 to 0.7 μm. As for the laser procedure, the preliminary spectral samples characterization helps to choose the correct laser source wavelength for processing inside the sample. Section 3.4 discusses plasmonic features.

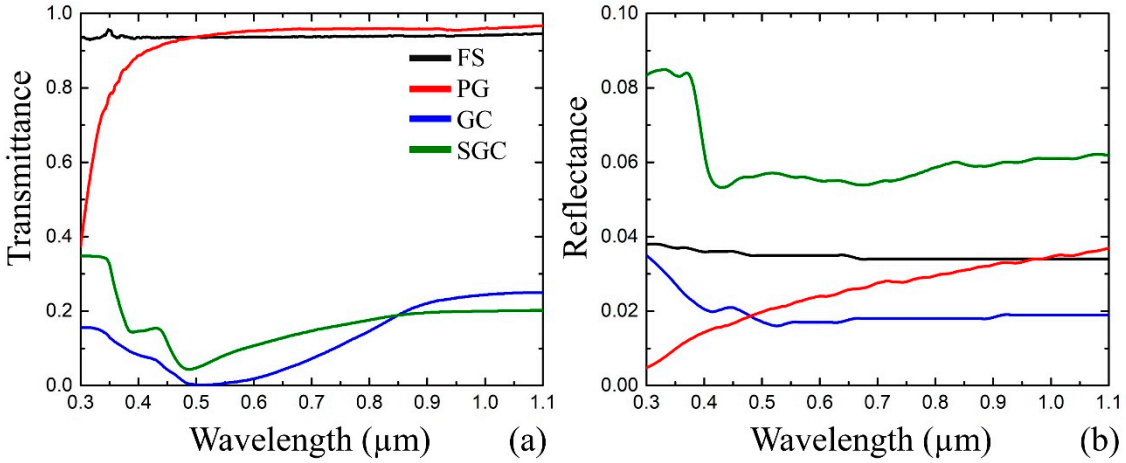

Figure 1. (**a**) Measured transmittance and (**b**) reflectance spectra of porous glass (PG) (red line), glass composite (GC) (blue line), sintered GC (SGC) (green line), and fused silica (FS) (black line) in the range from 0.3 to 1.1 μm.

2.2. Laser Irradiation

A commercially available CW fiber laser source is chosen to induce both silica matrix and salt mixture modification triggering local optical changes inside GC. The wavelength (λ_{laser} = 1064 nm) differs from the maximum absorption of GC (Figure 1a) and enables gentle processing. Figure 2 schematically shows the setup used for the experiment. The CW fiber laser source provides the maximum power P_0 = 20 W in the TEM_{00} mode with beam quality M^2 = 2, while the radiation divergence equals 20 mrad and the beam size incident on an objective equals 8 mm. The laser stabilizes within 100 microseconds after turning it on. The objective (10×, NA = 0.25) is used to achieve the laser beam waist diameter ($2\omega_0$) to be equal to 15 μm and its length 40 μm. The beam waist is located at 500 μm below the GC surface. Incident laser power (P_0) and the transmitted one (P_1) are both registered by Gentec Solo PE-2M (Lake Oswego, OR, USA) optical power meters equipped with UP19K-110F-H9 pyroelectric power detectors (Lake Oswego, OR, USA). The uncertainty of the power meter calibration is ±2.5%. Section 2.3 discusses the real-time control of plasmonic structure fabrication applied here.

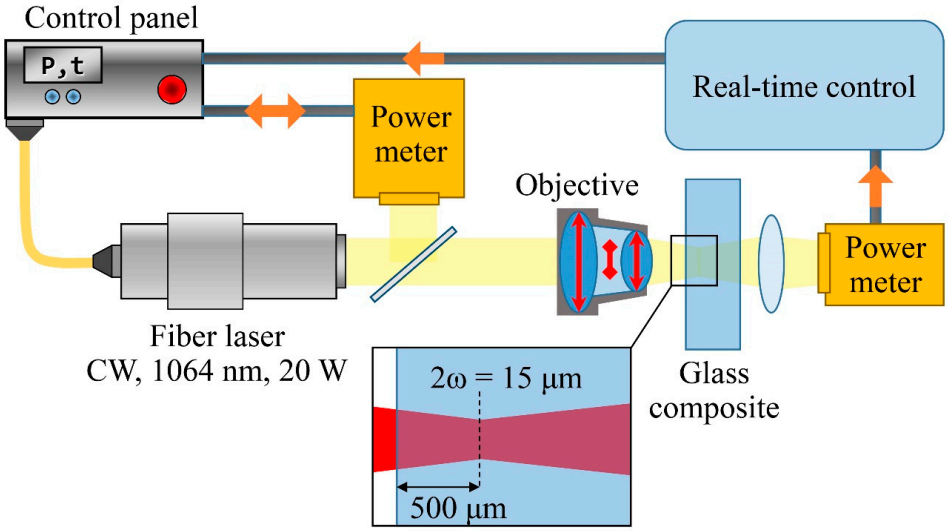

Figure 2. Schematics of the experimental setup for micro-sized plasmonic structures fabrication inside GC.

2.3. Real-Time Control: Background

The proposed real-time control procedure aims to optimize the laser parameters of GC irradiation by providing the laser power feedback for fabricating the buried microstructure with desirable spectral characteristics. Figure 3 schematically shows the procedure and it involves the following steps.

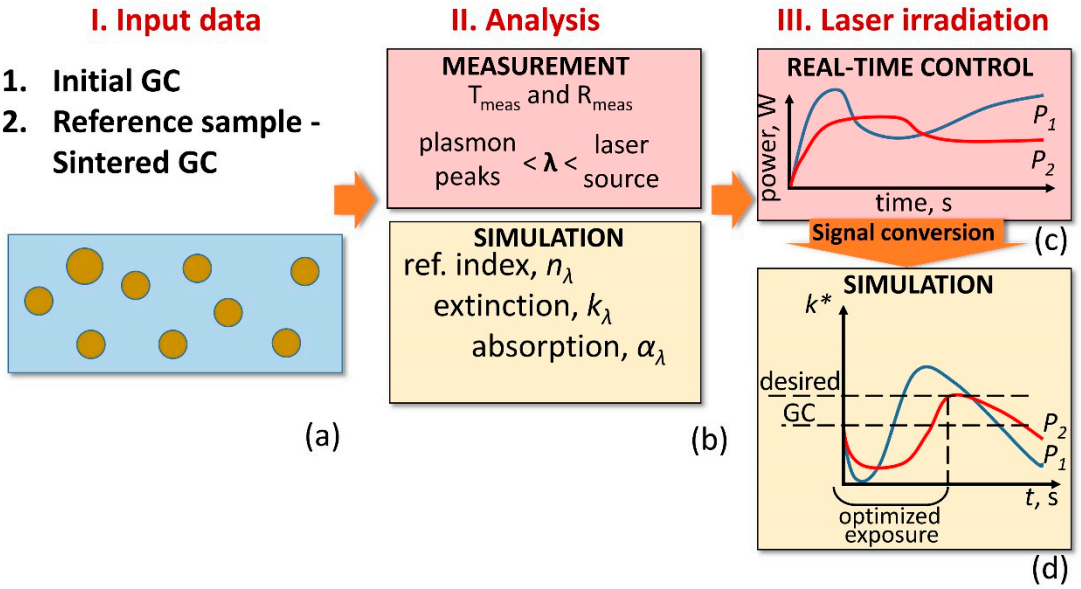

Figure 3. Schematics of the optimization procedure used to fabricate structures with desired optical properties inside GC: (**a**) input data as the sample to irradiate and the reference one—SGC; (**b**) measurement and simulation of the samples optical characteristics; (**c**) real-time monitoring of transmitted laser power; and (**d**) mathematical conversion of the registered laser power to extinction (k^*) behaviour at a specific period of the irradiation time.

(i) First, we set input data: the material to irradiate – GC, and the reference sample, which possesses the desired optical properties of the structure to fabricate, in our case it is SGC (Figure 3a).

(ii) Subsequently, the transmittance and reflectance of the samples are measured (Figure 3b). The registration range covers possible plasmonic peaks and applied laser wavelength. Simultaneously, the main optical constants, namely, the absorption (α_λ), extinction (k_λ), and refractive index (n_λ) are estimated by the mathematical simulation. The optical properties of the structure to fabricate are homologated with the reference sample.

(iii) Next, GC laser irradiation is accompanied by the incident and transmitted laser power monitoring (Figure 3c).

(iv) Since the structure is fabricated inside GC, the transmitted laser power brings the key optical parameter, such as an extinction (k^*). This enables us to leap ahead to convert the transmitted power signal into k^* behaviour at a specific period of the irradiation time through the mathematical simulation (Figure 3d). Laser irradiation activates photo-thermo-chemical mechanisms that dramatically deviate the extinction curve and confuses the exposure time. Hence, it is also important to describe the mechanisms that are involved for any new glass composite to irradiate.

(v) Afterwards, the user sets the desired extinction for the structure to fabricate. For example, in the experiment, we associate the desired extinction with one of SGC (k_λ) estimated in the second step. The convergence of both extinction values—the initial and reference one—shows the required exposure time and laser power to fabricate a plasmonic structure.

After spectral investigation of the fabricated structure, it becomes possible to estimate the size, concentration, and chemical composition of the secondary phase across the structure through the

simulation that is based on the effective medium theory [19,25]. It is worth noting that this investigation is performed without fragmentation of the structure. The details are presented in Section 3.4.

3. Results and Discussion

3.1. Results of Glass Composite Laser Processing

Upon laser irradiation of GC, a modified region appears and it is clearly visible for power density in the range from 6.3×10^5 to 1.9×10^6 W/cm^2. The formed regions are characterized by darkening in the exposure area under a microscope (Figure 4a). While displacing the image plane of the microscope, the modified region has the central part and the periphery (Figure 4b). The lateral size of the region is about 150 µm. The image indicates higher density in the central part than that in the non-irradiated region. It seems like a focused laser radiation forms a heat point source inside GC, which leads to the secondary phase redistribution across the irradiated region with the spaces in the central part [26] (Figure 4b). The subsequent shift of the image plane of the microscope shows the ability to recreate the image of the objects located on the optical axis. Since the diaphragm of the microscope lighting system is observed (Figure 4c), the fabricated structure plays the role of a microlens, where density is increased in the central part. Section 3.4 discusses the secondary phase determined by spectral investigation.

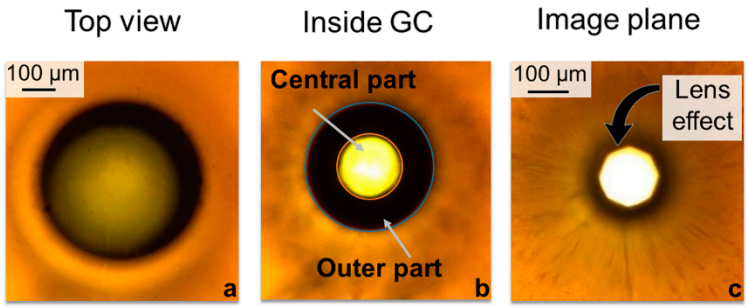

Figure 4. Laser-modified region fabricated at laser exposure of 15 s with power 13 W inside GC micro-photos captured in the transmission light at different position of the microscope image plane: (**a**) surface of modified region, (**b**) central part, and (**c**) under the region in its image plane.

The size of the structure depends on laser power and exposure time. In the case of P_0 = 9.6 W, we experimentally observe that the diameter shrinks from 2 to 2.5 times during 15 s (Figure 5). Interestingly, over the next 5–10 s, the outer part size decreases by 1.5 times, i.e., it is practically restored. Consequently, all of the fabricated structures consist of two sections: optically transparent at the centre and obscured at the periphery.

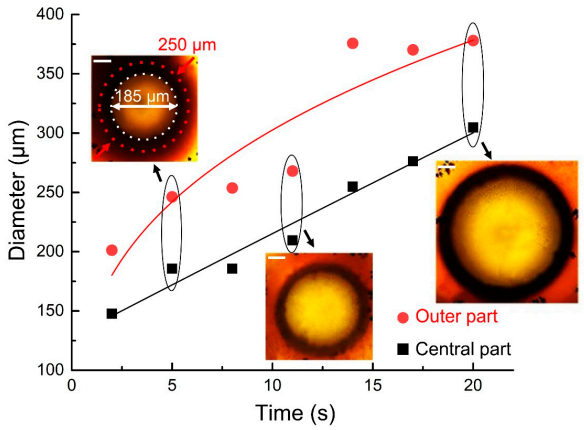

Figure 5. Time evolution of the fabricated structure centre and outer diameter in the process of 20 s laser exposure at P_0 = 9.6 W. Scale bar equals to 50 µm.

3.2. Laser Power Monitoring and Mechanism Description

The registration of the incident (P_0) and transmitted (P_1) laser powers shows the "breathing effect" in the transmitted power signal (Figure 6), which distinguishes three stages of the creation of the modified region. Stage I starts from the beginning of laser irradiation and captures an abrupt rise in the transmitted power for several seconds. Subsequently, transparency increases more slowly for 5–7 s. It continues for a longer time (12 s) for the lowest power (P_0 = 6.1 W). A sharp decrease in the transmission takes place during stage II. The GC darkening was clearly observed at this stage that lasts for 7–15 s and is shorter for larger laser powers. During stage III (after the delay of 16 s for P_0 = 7.9 W and 18 s for P_0 = 9.6 W) a partial transmission recovery is observed at laser power above 7 W. The recovery takes more time for lower laser powers.

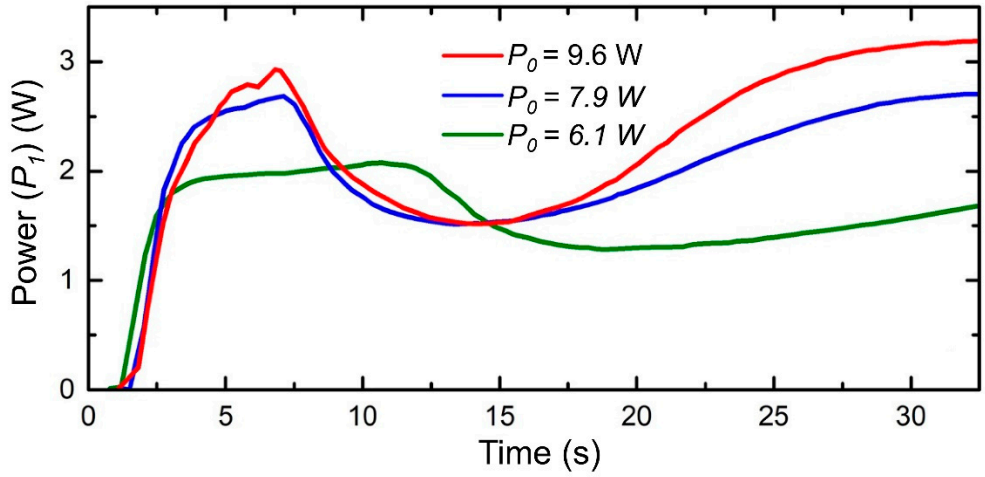

Figure 6. Time-evolution of the transmitted laser power (P_1) during the structure fabrication, while the incident, P_0, equals to 6.1 W (green), 7.9 W (blue), and 9.6 W (red).

We would like to remind that the final structure consists of several well-pronounced regions, as follows: the central part that is almost optically transparent and the heavily darkened periphery parts (Figure 4b). A better understanding of the mechanisms of such a structure formation is needed in order to understand the nature of the secondary phase redistribution generation and to determine the features homologated with the end of the structure fabrication. Generally, laser irradiation of a glass composite initiates a combination of the thermally activated nanoparticle growth and ion migration processes determining the optical properties of the composite material [27]. Albeit light absorption by metallic clusters is negligible for the considered laser wavelength (our laser operates at 1064 nm), our GC sample is locally heated inside, which is sufficient for material thermal expansion, sintering/densification, softening, etc. A photo-thermo-chemical mechanism is involved because the GC are photosensitive and the absorbed laser radiation heats the secondary phase.

Based on the laser power feedback, we identify the possible reasons for the GC optical properties changes, as follows: (i) halides decomposition to ions and water removal; (ii) a subsequent temperature increase leads to the nanoporous framework densification that also slows the ion migration outwards to the periphery; and, (iii) the ions thermal diffusion leads to nanoparticles growth around the laser-irradiated zone. In the central part, a small number of nanoparticles remains anyway, even with the laser source turned off, since the lifetime of the laser-induced thermal field is sufficient for thermal diffusion.

3.3. Simulation of Optical Properties

In the case of GC sintered in a furnace, the modification processes take place sequentially across the entire sample and they are determined by both temperature and exposure time. On the contrary, laser irradiation accelerates and localizes the processes in the interaction zone. The primary simulation

of optical properties is performed for SGC, since the final optical properties of the structure to fabricate equal SGC. Pure FS and PG are applied as samples to compare. The absorption coefficient (α_λ), extinction (k_λ), and material refractive index (n_λ) are derived from the measured T_{meas} and R_{meas} (Figure 1), while taking the samples thickness (h) into account [28]:

$$T_{meas} = \frac{I_T}{I_0} = \frac{(1-R_\lambda)^2 \exp(-\alpha_\lambda h)}{1-R_\lambda^2 \exp(-2\alpha_\lambda h)} \quad (1)$$

$$R_{meas} = \frac{I_R}{I_0} = R_\lambda[1 + T_{meas} \exp(-\alpha_\lambda h)] \quad (2)$$

where λ is the laser radiation wavelength, R_λ is inner reflection determined by the Fresnel equation [29] when considering the samples location in air:

$$R_\lambda = \frac{(n_\lambda + 1)^2 + k_\lambda^2}{(n_\lambda - 1)^2 + k_\lambda^2} \quad (3)$$

The absorption coefficient is calculated based on Equations (1) and (2), as follows:

$$\alpha_\lambda = \frac{1}{h} \ln\left(L + \sqrt{L^2 + R_{meas}^2}\right) \quad (4)$$

where $L = (1 - R_{meas})^2/(2T_{meas})$. Since $k_\lambda = \alpha_\lambda \lambda/4\pi$, we estimate the extinction (Figure 7a). Currently, we suppose the internal and external reflection coefficients are such that the refractive index (n_λ) can be evaluated, as follows (Figure 7b):

$$n_\lambda = A + \sqrt{A^2 - k_\lambda^2 - 1} \quad (5)$$

where $A = (1 + R_{meas})/(1 - R_{meas})$.

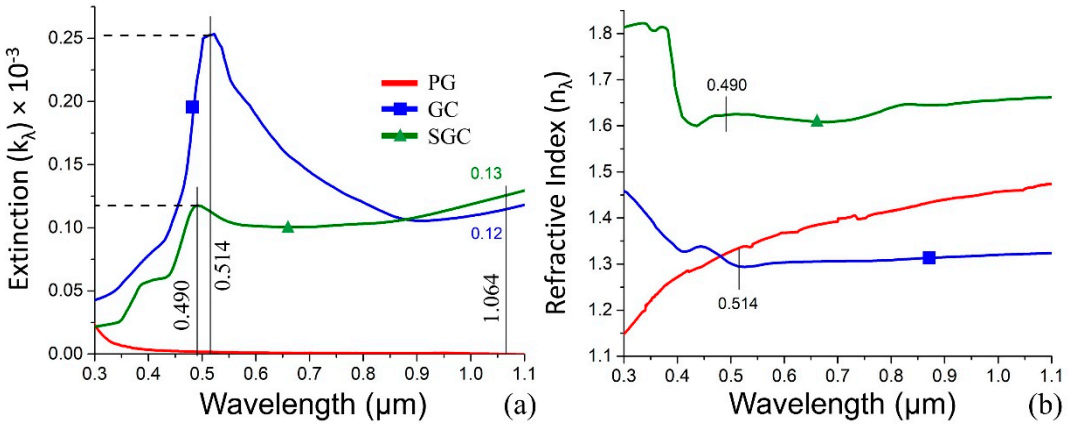

Figure 7. The simulation results: (**a**) the extinction, (**b**) refractive index for PG (red line), GC (blue line), and SGC (green line).

The performed simulations show the peak wavelength and its shift from 514 nm to 490 nm after GC sintering (Figure 7). However, the extinction peak dramatically decreases (Figure 7a).

It is reasonable to suppose that the absorption of SGC is higher and the secondary phase volume was increased, which is also confirmed by the increased SGC refractive index (Figure 7b). The PG curve is presented here just to show the absence of any peak. The simulation shows that the extinction function is more informative when compared to the refractive index function. GC and SGC extinctions obtained for 1.064 μm allow for one to associate them as the bottom and upper limit for the structure to fabricate.

The calculations of the extinction coefficient are performed for the transmitted laser power to obtain the time dependent dynamic extinction change (k^*) for the constant laser wavelength of l064 nm. Figure 8 demonstrated that the k^* curves change as a function of the incident laser power. The previously estimated extinction coefficients for GC and SGC are also shown in the Figures by solid lines. The intersection of these curves corresponds to the material phase shift state changing from GC to SGC. In our case, the extinction of the fabricated structure has to converge the initial glass extinction and go to SGS one.

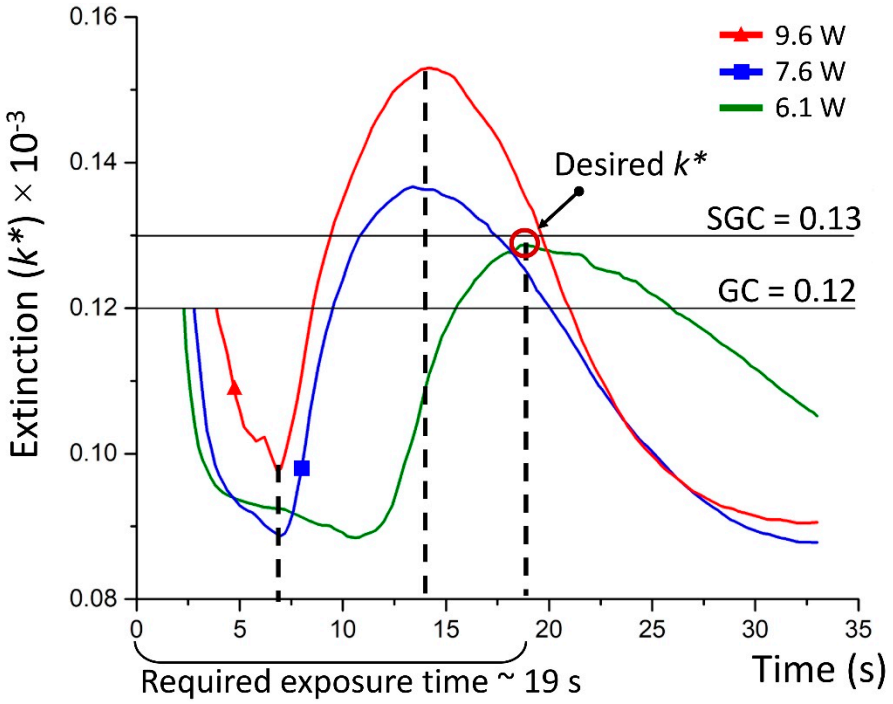

Figure 8. Simulated time dependent extinction (k^*) changes during laser irradiation at different incident power: 9.6 W (red curve), 7.9 W (blue curve), and 6.1 W (green curve).

The k^* dynamics is worth investigating (Figure 8). For the first 7 s we notice a sharp drop indicating the second phase, where halogenides dissipate in the irradiation region, i.e., silver bromide and iodide are decomposed. Subsequently, the temperature arises exceeding 400 °C, which enables free ions to collect in a nanoparticle. The nanoparticles growth provides greater absorption, which is seen in the curve increasing from 7 till 12 s. The increased absorption corresponds to the temperature increase until the critical value, preventing nanoparticles dissipation. Thus, k^* decreases again, crossing SGC extinction state and then after a few seconds the GC state. All of this is true for the incident power equals 7.9 and 9.6 W. The opposite situation takes place for the smallest power 6.1 W, where the extinction goes to SGC one. For this, the laser exposure time equals to ~17 s. Thus, we obtain the desirable material state and there is no need for further laser irradiation. As a result, we suggest feedback based on the transmitted laser power to optimize the laser processing of GC.

We note that the main purpose of the laser source is to establish a sustainable heat source. The heat source activates the nanoparticles growth. Thus, the suggested procedure can be adopted for various types of laser irradiation, such as continuous radiation [30], as well as for a pulsed laser irradiation [31,32]. Another point is that a partial sample transmission is required to provide the registration of the transmitted laser power.

3.4. Plasmonic Properties and Nanoparticles Properties Simulation

Figure 9a shows the micro-spectroscopy results obtained for all zones of the fabricated structure. The presence of salt mixture in the nanoporous framework results in the plasmonic response appearance that is characterized by the absorption peak at λ = 509 nm. The obtained spectrum clearly indicates the presence of the secondary phase across the fabricated buried structure with different volume/concentration: central, 1st, and 2nd zones. The farther from its centre, the more pronounced and shifted the peak is. The larger is the nanoparticle size in the dielectric medium, the more the peak is shifted to the blue region. Spectral analysis across the structure shows a set of coaxial spheroids, where the outer is formed from the secondary phase with different-sized nanoparticles. Thus, secondary phase migration toward the periphery of the laser-affected volume is obvious.

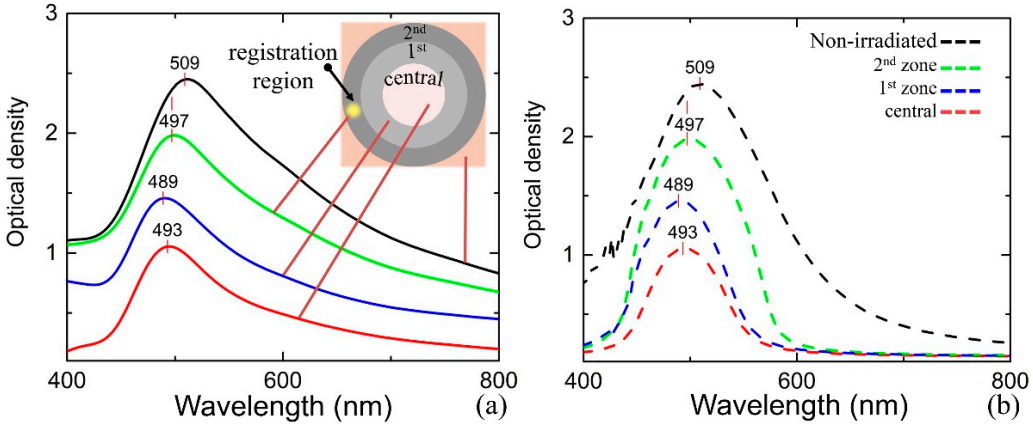

Figure 9. (**a**) Optical density spectra for the initial sample and measured at several distances from the centre of the fabricated structure. Inserted scheme represents the top view of the structure fabricated at 15 W and 20 s. (**b**) Simulation results providing the best fit to the experimental and yielding the mean nanoparticle diameter of 11 nm for the central part (optical density is peaked at 493 nm), 14 for the next ring (optical density is peaked at 489 nm), 30 nm (at 497 nm), and 4 nm for the outer region (at 509 nm).

Based on the EMT [19,25], it becomes possible to simulate the spectra for each zone in the sample: central, the 1st one, the 2nd one, and the unirradiated one. A careful tuning of chemical composition, nanoparticles size, and metal volume ratio for effective mediums of each zone in the model allows for us to fit the measured spectra. The initial sample properties are determined based on the fitting of the following measurements [33]: dispersion of the pore size distribution, dispersion of nanoclusters distribution (Figure 10), mass fraction of the secondary phase, the initial concentration of the secondary phase atoms, and the spectral characteristics in the various parts of the sample. In the simulation, we consider the plasmon resonance from the nanoparticle assembly (Ag, AgCl, AgBr, AgI, Ag_2O) distributed in a dielectric medium (Table 1). The initial composition of the secondary phase included silver halides in equal proportions according to the impregnation condition.

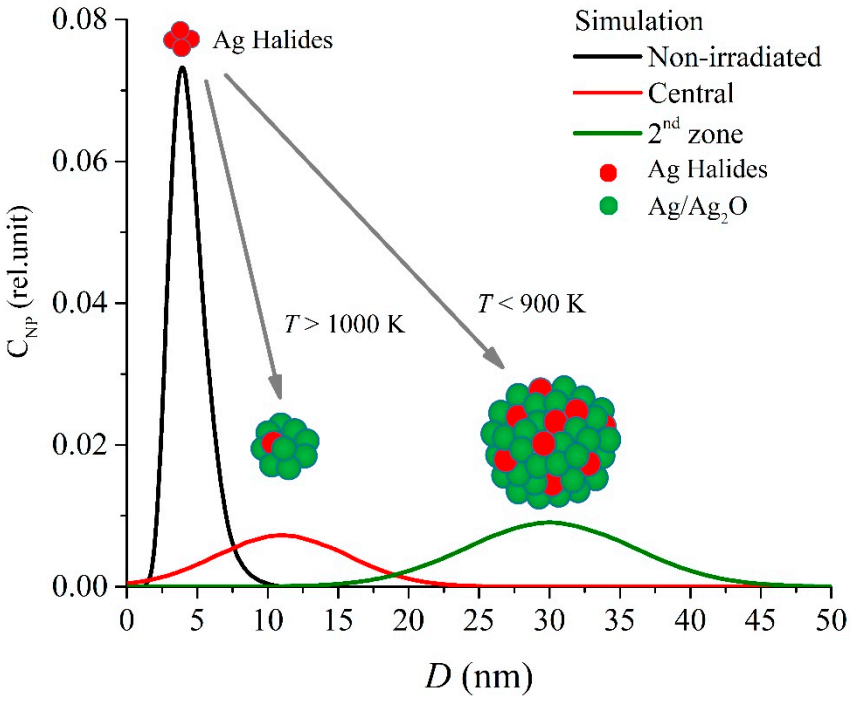

Figure 10. Simulated size (D) distribution of nanoparticles (concentration, C_{NP}) in the sample for the non-irradiated zone (C_{NP} = 0.073, D ~ 4 nm) and the fabricated structure: its central part (C_{NP} = 0.0072, D ~ 10 nm) and the 2nd zone (C_{NP} = 0.0090, D ~ 30 nm).

Table 1. Chemical composition of the secondary phase in the nanoporous framework before and after laser irradiation.

Zone	Cu	Cu_2O	Ag	Ag_2O	AgCl	AgBr	AgI	N_2	O_2	Ar	H_2O
Initial GC											
Non-irradiated	1	2	1	0	32	32	32	64	17.2	0.8	18
Fabricated structure											
Center			83	14	0	0	0				
1st	1	2	32	20	25	15	5	78.1	21	0.9	0
2nd			16	6	30	30	15				

The following procedure of the concentration adjustment is then applied to simulate the nanocomposite optical properties. The GC consists of the framework dielectric function (ε_m) and the secondary phase (ε_{ph}), including its volume fraction (ν_{ph}). The dielectric function of the effective medium holds true $\varepsilon_{eff} = (n_\lambda + ik_\lambda)^2 = f(\nu_{ph}, \varepsilon_{ph}, \varepsilon_m)$. An approximation of isolated nanoparticles is used here. In this case, the distance between particles is larger than their size ($d >> 2r_{Np}$). The Bruggeman approximation is chosen as the most suitable model presentation [19]. The complex GC description is accomplished by the Bergmann equation [25,33]. The thickness of the model sample equals 90 μm, corresponding to a photometric layer of the microscope-spectrometer.

The same procedure is performed for the laser-irradiated region, which consisted of the central part, the 1st, and the 2nd zones. However, the chemical composition of each zone depends on the behaviour of silver halides during laser-induced heating. Therefore, the following conditions are applied to tune the chemical composition for each zone (Table 1). In the central zone, when considering the sintering of the nanoporous matrix in the beam waist, which was discussed above, the transition temperature (up to 1000–1300 K) is achieved [34]. Thus, such silver halides are thermally decomposed, according to the handbook [35], as following: for AgI at 825 K, AgBr at 970 K, and AgCl at 1313 K. The decomposition leads to ions formation with following combination into nanoparticles. For the 1st

and the 2nd zones, which are far from the beam waist, the temperature was lower. As a result, the most heat resistant silver halide (AgCl) remains practically unchanged. Thus, the initial nanoporous framework of these zones is filled with silver nanoparticles, which diffused from the central part, and with the silver halides (Table 1).

The optical density registration for each zone (Figure 9a) confirms the above discussion. Unlike silver nanoparticles, its oxide and halides do not have a pronounced plasmon resonance in the optical visible wavelength range. The silver oxide resembles to a semiconductor in view of its electronic structure and optical properties [36]. In fact, properties, such as concentration (N), effective mass (m), and relaxation time (τ), are smaller for silver halides and its oxide when compared to the pure silver (Table 2). The wavelength peak shifts to the IR region as well as its intensity decreases as a result of an increase in the fraction of silver halides. Thus, the peak position and its intensity are the reference characteristic for the estimation of the chemical composition of the secondary phase. The chemical composition (Table 1) in the model is corrected to fit the simulated spectrum to the measured one in the spectral range 0.3–1.1 μm (Figure 9b). We can also see the plasmon resonance width in the simulated spectra, which turned out to be smaller when compared to the experimental data. Such a difference is probably due to the light scattering on the nanoporous framework, which is disregarded in the present model.

Table 2. Values of parameters for different components of the secondary phase.

	Cu	**Cu_2O**	**Ag**	**Ag_2O**	**AgCl**	**AgBr**	**AgI**
N (cm^{-3})	8.47×10^{22}	5.47×10^{22}	5.86×10^{22}	2.86×10^{22}	2.59×10^{19}	1.85×10^{18}	1.4×10^{20}
m	1.49	0.98	0.55	0.7	0.25	0.177	0.147
τ (s)	8.52×10^{-15}	1.18×10^{-14}	9.20×10^{-15}	1.10×10^{-14}	1.0×10^{-4}	5.0×10^{-8}	1.0×10^{-7}
v_F (m/s)	1.287×10^6	1.466×10^6	1.876×10^6	1.568×10^6	2.685×10^6	2.924×10^6	3.312×10^6

The nanocluster concentration is calculated as a volume ratio of the secondary phase by using the following distance-depending parameters: 0.41% in the initial PG, 0.1% in the central part of the laser-modified region, and 0.38% in the surrounding part. Thus, nanoparticle diameter is found to range from 11 to 30 nm inside and around the laser-affected zone, whereas this size is as small as 4 nm in the unmodified PG plate part.

The calculations of the spectral characteristics are based on the effective dielectric function, ε_{eff} [34]. This function accounts for the dielectric properties of the secondary phase in the form of silver nanoparticles, silver oxide, and halides in different proportions, as well as the host medium. The dielectric function of the secondary phase can be expressed in terms of the incident radiation, λ [37,38]:

$$\varepsilon_{ph}(\lambda) = \varepsilon_{Bulk}(\lambda) + \varepsilon_{Shape}(\lambda) + \varepsilon_{Plasm}(\lambda) \quad (6)$$

The first term describes the properties of the bulk material:

$$\varepsilon_{Bulk}(\lambda) = \sum_{i=1}^{I} \mu_i \varepsilon_{Com}(\lambda)_i \quad (7)$$

where μ_i is the mass fraction of the components in the composition of nanoparticles. The values of $\varepsilon_{\mathrm{Com}}(\lambda)$ for all components are taken from Ref. [39].

The second term accounts for the electronic properties of the nanoparticles with radius r_{NP}

$$\varepsilon_{Shape}(\lambda) = \frac{e^2 \lambda r_{NP}}{2\pi c \varepsilon_0} \sum_{i=1}^{I} \frac{\mu_i n_i \lambda}{m_i v_{F,i}(2\pi c \mu_i \tau_i + i\lambda)} \quad (8)$$

where r_{NP} = 0.5·D, e is the elementary charge, c is the speed of light in vacuum, ε_0 is the dielectric constant, and n, m, τ, v_F are the concentration, effective mass, relaxation time, and velocity near the Fermi level for free electrons, respectively. Table 2 presents the parameters used in the simulation.

The determined ε_{eff} allows for us to recover the transmission spectra (T_s) by Equation (1), where absorption coefficient is used as $\alpha = (4\pi/\lambda)Im((\varepsilon_{eff})^{0.5})$. The final optical density plot is simulated as $OD = \lg(1/T_s)$ (Figure 9b).

4. Conclusions

In conclusion, we have developed and described a novel real-time control procedure combining both experimental measurements and simulation to fabricate micro-sized structures inside GC. In particular, we have simulated the time dependent changes in the optical properties of the laser-irradiated nanoporous glass composite. In the proposed procedure, only the experimentally obtained transmitted laser power and numerically calculated time-dependent optical properties are used in order to optimize laser irradiation parameters. Subsequently, the optical non-contact methods have been applied to investigate the fabricated structure. The EMT is used to connect the measured spectrum from each layer of the fabricated region and to estimate size, concentration, and chemical composition of the secondary phase across the layer. Every new glass composite to irradiate requires the mechanism interpretation as an integral part of the procedure. All of the involved steps make the procedure suitable for an effective monitoring of the plasmonic properties of the fabricated structures.

In addition, a curious "breathing effect" of transmittance has been demonstrated and explained. On one hand, the measured time-evolutions of the transmitted laser power correlate to the transitional material changes, such as softening, pore shrinking, dilatation, and cavitation. As a result, the porous structure is firstly erased and then renewed in the laser-modified volume. Shrinking pores prevent metallic species escape, while opening pores allow this process again. On the other hand, these results are also affected by the evolution of bimetallic nanoparticles that grow mostly at the periphery of the hot region at moderate laser heating. The final laser-induced structure, being strongly dependent on laser power and laser irradiation time, has been represented by a set of coaxial spheroids. If laser energy is high enough, the outer spheroidal shell is mostly composed of the secondary phase. In addition to the phase transitions and pore renewal, the formation of the observed microstructure has been attributed to nanocluster formation and metallic species migration that arise from the laser-generated temperature field.

The fabrication of such buried microstructures in a glass composite is particularly promising for numerous photonic and plasmonic applications.

Author Contributions: Conceptualization, M.M.S. and T.E.I.; methodology, M.M.S.; software, P.V.V.; validation, M.M.S., R.A.Z.; formal analysis, P.V.V.; investigation, M.M.S., R.A.Z.; resources, G.K.K.; data curation, P.V.V.; writing—original draft preparation, M.M.S., R.A.Z.; writing—review and editing, T.E.I.; visualization, R.A.Z.; supervision, T.E.I.; project administration, R.A.Z.; funding acquisition, M.M.S. All authors have read and agreed to the published version of the manuscript.

Funding: The study is funded by the grant of Russian Science Foundation (project No. 19-79-10208).

Acknowledgments: Authors are grateful to T.V. Antropova and M.A. Girsova from the laboratory of physical chemistry of glass (Institute of Silicate Chemistry of Russian Academy of Sciences, St. Petersburg) for the GC samples preparation.

Conflicts of Interest: The authors declare no conflict of interest. The funders had no role in the design of the study; in the collection, analyses, or interpretation of data; in the writing of the manuscript, or in the decision to publish the results.

References

1. Singh, S.P.; Karmakar, B. Controlled oxidative synthesis of Bi nanoparticles and emission centers in bismuth glass nanocomposites for photonic application. *Opt. Mater.* **2011**, *33*, 1760–1765. [CrossRef]
2. Schneider, R.; Schneider, R.; de Campos, E.A.; Mendes, J.B.S.; Felix, J.F.; Santa-Cruz, P.A. Lead–germanate glasses: An easy growth process for silver nanoparticles and their promising applications in photonics and catalysis. *RSC Adv.* **2017**, *7*, 41479–41485. [CrossRef]

3. Abou Khalil, A.; Bérubé, J.-P.; Danto, S.; Desmoulin, J.-C.; Cardinal, T.; Petit, Y.; Vallée, R.; Canioni, L. Direct laser writing of a new type of waveguides in silver containing glasses. *Sci. Rep.* **2017**, *7*, 11124. [CrossRef] [PubMed]
4. Nedyalkov, N.; Dikovska, A.; Koleva, M.; Stankova, N.; Nikov, R.; Borisova, E.; Genova, T.; Aleksandrov, L.; Iordanova, R.; Terakawa, M. Luminescence properties of laser-induced silver clusters in borosilicate glass. *Opt. Mater.* **2020**, *100*, 109618. [CrossRef]
5. de Castro, T.; Fares, H.; Khalil, A.A.; Laberdesque, R.; Petit, Y.; Strutinski, C.; Danto, S.; Jubera, V.; Ribeiro, S.J.L.; Nalin, M.; et al. Femtosecond laser micro-patterning of optical properties and functionalities in novel photosensitive silver-containing fluorophosphate glasses. *J. Non-Cryst. Solids* **2019**, *517*, 51–56. [CrossRef]
6. Heinz, M.; Srabionyan, V.V.; Avakyan, L.A.; Bugaev, A.L.; Skidanenko, A.V.; Kaptelinin, S.Y.; Ihlemann, J.; Meinertz, J.; Patzig, C.; Dubiel, M.; et al. Formation of bimetallic gold-silver nanoparticles in glass by UV laser irradiation. *J. Alloys Compd.* **2018**, *767*, 1253–1263. [CrossRef]
7. Zhang, Y.; Zhang, Q.; Ouyang, X.; Lei, D.Y.; Zhang, A.P.; Tam, H.-Y. Ultrafast light-controlled growth of silver nanoparticles for direct plasmonic color printing. *ACS Nano* **2018**, *12*, 9913–9921. [CrossRef]
8. Capoen, B.; Chahadih, A.; El Hamzaoui, H.; Cristini, O.; Bouazaoui, M. Laser-induced growth of nanocrystals embedded in porous materials. *Nanoscale Res. Lett.* **2013**, *8*, 1–10. [CrossRef]
9. Antropova, T.; Girsova, M.; Anfimova, I.; Drozdova, I.; Polyakova, I.; Vedishcheva, N. Structure and spectral properties of the photochromic quartz-like glasses activated by silver halides. *J. Non-Cryst. Solids* **2014**, *401*, 139–141. [CrossRef]
10. Iskhakova, L.D.; Mashinsky, V.M.; Milovich, F.O.; Velmiskin, V.V.; Plastinin, E.A.; Firstov, S.V.; Lukashova, M.V.; Somov, P.A.; Dianov, E.M. Microstructure, composition, and luminescent properties of bismuth-doped porous glass and optical fiber preforms. *J. Non-Cryst. Solids* **2019**, *503*, 28–35. [CrossRef]
11. Santos, E.d.B.; Sigoli, F.A.; Mazali, I.O. Metallic Cu nanoparticles dispersed into porous glass: A simple green chemistry approach to prepare SERS substrates. *Mater. Lett.* **2013**, *108*, 172–175. [CrossRef]
12. Teng, Y.; Zhou, J.; Lin, G.; Hua, J.; Zeng, H.; Zhou, S.; Qiu, J. Ultrafast modification of elements distribution and local luminescence properties in glass. *J. Non-Cryst. Solids* **2012**, *358*, 1185–1189. [CrossRef]
13. Sergeev, M.M.; Kostyuk, G.K.; Zakoldaev, R.A.; Girsova, M.A.; Anfimova, I.N.; Antropova, T.V. Organization of silver nanoclusters in porous glass bulk by laser irradiation. *Glass Phys. Chem.* **2017**, *43*, 395–398. [CrossRef]
14. Goutaland, F.; Sow, M.; Ollier, N.; Vocanson, F. Growth of highly concentrated silver nanoparticles and nanoholes in silver-exchanged glass by ultraviolet continuous wave laser exposure. *Opt. Mater. Express* **2012**, *2*, 350–357. [CrossRef]
15. Seifert, G.; Stalmashonak, A.; Hofmeister, H.; Haug, J.; Dubiel, M. Laser-Induced, Polarization Dependent Shape Transformation of Au/Ag Nanoparticles in Glass. *Nanoscale Res. Lett.* **2009**, *4*, 1380. [CrossRef] [PubMed]
16. Garnett, J.M., XII. Colours in metal glasses and in metallic films. *Philos. Trans. R. Soc. London. Ser. Acontaining Pap. A Math. Or Phys. Character* **1904**, *203*, 385–420. [CrossRef]
17. Bergman, D.J. The dielectric constant of a composite material—A problem in classical physics. *Phys. Rep.* **1978**, *43*, 377–407. [CrossRef]
18. Pinchuk, A.; Kreibig, U.; Hilger, A. Optical properties of metallic nanoparticles: Influence of interface effects and interband transitions. *Surf. Sci.* **2004**, *557*, 269–280. [CrossRef]
19. Sturm, J.; Grosse, P.; Theiss, W. Effective dielectric functions of alkali halide composites and their spectral representation. *Zeitschrift für Physik B Condens. Matter* **1991**, *83*, 361–365. [CrossRef]
20. Drozdova, I.A.; Antropova, T.V.; Tolkachev, M.D. Application of electron microscopy methods to the study of porous and quartz-like glasses. *Opt. Appl.* **2005**, *35*, 709–715.
21. Kreisberg, V.; Antropova, T.; Kalinina, S. Formation of micro-and mesoporous substructures in the course of the leaching process of two-phase alkali borosilicate glass. *Glass Phys. Chem.* **2014**, *40*, 384–387. [CrossRef]
22. Kreisberg, V.; Antropova, T.; Kalinina, S. Effect of the composition and conditions of the synthesis of porous glass on their micro-and mesoporous structures. *Glass Phys. Chem.* **2014**, *40*, 501–512. [CrossRef]
23. Antropova, T.; Girsova, M.; Anfimova, I.; Drozdova, I. Spectral properties of the high-silica porous glasses doped by silver halides. *J. Lumin.* **2018**, *193*, 29–33. [CrossRef]
24. Girsova, M.; Drozdova, I.; Antropova, T. Structure and optical properties of photochromic quartz-like glass doped with silver halides. *Glass Phys. Chem.* **2014**, *40*, 162–166. [CrossRef]

25. Malasi, A.; Kalyanaraman, R.; Garcia, H. From Mie to Fresnel through effective medium approximation with multipole contributions. *J. Opt.* **2014**, *16*, 065001. [CrossRef]
26. Kriegel, I.; Scotognella, F.; Manna, L. Plasmonic doped semiconductor nanocrystals: Properties, fabrication, applications and perspectives. *Phys. Rep.* **2017**, *674*, 1–52. [CrossRef]
27. Nikonorov, N.; Sidorov, A.; Tsekhomskii, V. *Silver Nanoparticles in Oxide Glasses: Technologies and Properties*; IntechOpen: London, UK, 2010; Volume 177. [CrossRef]
28. Malerba, C.; Biccari, F.; Ricardo, C.L.A.; D'Incau, M.; Scardi, P.; Mittiga, A. Absorption coefficient of bulk and thin film Cu_2O. *Sol. Energy Mater. Sol. Cells* **2011**, *95*, 2848–2854. [CrossRef]
29. Kasap, S.; Capper, P. *Springer Handbook of Electronic and Photonic Materials*; Springer: Cham, Switzerland, 2017. [CrossRef]
30. Tite, T.; Ollier, N.; Sow, M.C.; Vocanson, F.; Goutaland, F. Ag nanoparticles in soda-lime glass grown by continuous wave laser irradiation as an efficient SERS platform for pesticides detection. *Sens. Actuators B Chem.* **2017**, *242*, 127–131. [CrossRef]
31. Siozios, A.; Koutsogeorgis, D.; Lidorikis, E.; Dimitrakopulos, G.; Pliatsikas, N.; Vourlias, G.; Kehagias, T.; Komninou, P.; Cranton, W.; Kosmidis, C. Laser-matter interactions, phase changes and diffusion phenomena during laser annealing of plasmonic AlN: Ag templates and their applications in optical encoding. *J. Phys. D Appl. Phys.* **2015**, *48*, 285306. [CrossRef]
32. Chiasera, A.; Macchi, C.; Mariazzi, S.; Valligatla, S.; Lunelli, L.; Pederzolli, C.; Rao, D.N.; Somoza, A.; Brusa, R.S.; Ferrari, M. CO2 laser irradiation of GeO_2 planar waveguide fabricated by rf-sputtering. *Opt. Mater. Express* **2013**, *3*, 1561–1570. [CrossRef]
33. Kreisberg, V.A.; Antropova, T.V. Changing the relation between micro- and mesoporosity in porous glasses: The effect of different factors. *Microporous Mesoporous Mater.* **2014**, *190*, 128–138. [CrossRef]
34. Petrov, D.V.; Dyukareva, A.S.; Antropova, T.V.; Veiko, V.P.; Kostyuk, G.K.; Yakovlev, E.B. Surface sintering of porous glass plates under laser radiation. *Glass Phys. Chem.* **2003**, *29*, 456–460. [CrossRef]
35. Grigoriev, I.S.; Meæilikhov, E.Z. *Handbook of Physical Quantities*; CRC Press: Boca Raton, FL, USA, 1997.
36. Varkey, A.; Fort, A. Some optical properties of silver peroxide (AgO) and silver oxide (Ag_2O) films produced by chemical-bath deposition. *Sol. Energy Mater. Sol. Cells* **1993**, *29*, 253–259. [CrossRef]
37. Sancho-Parramon, J. Surface plasmon resonance broadening of metallic particles in the quasi-static approximation: A numerical study of size confinement and interparticle interaction effects. *Nanotechnology* **2009**, *20*, 235706. [CrossRef]
38. Cavaliere, E.; Benetti, G.; Van Bael, M.; Winckelmans, N.; Bals, S.; Gavioli, L. Exploring the optical and morphological properties of ag and Ag/TiO_2 nanocomposites grown by supersonic cluster beam deposition. *Nanomaterials* **2017**, *7*, 442. [CrossRef]
39. Smith, D.; Shiles, E.; Inokuti, M.; Palik, E. Handbook of optical constants of solids. *Handb. Opt. Constants Solids* **1985**, *1*, 369–406.